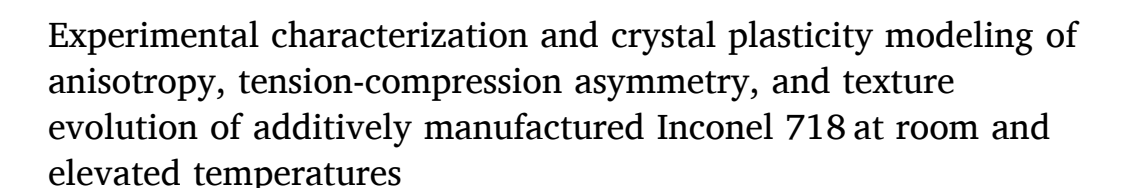
ELSEVIER

Contents lists available at ScienceDirect

International Journal of Plasticity

journal homepage: http://www.elsevier.com/locate/ijplas







Saeede Ghorbanpour ^a, Md Ershadul Alam ^b, Nicholas C. Ferreri ^a, Anil Kumar ^c, Brandon A. McWilliams ^d, Sven C. Vogel ^e, Jonathan Bicknell ^f, Irene J. Beyerlein ^b, Marko Knezevic ^{a,*}

- ^a Department of Mechanical Engineering, University of New Hampshire, Durham, NH, 03824, USA
- b Mechanical Engineering Department, Materials Department, University of California at Santa Barbara, Santa Barbara, CA, 93106, USA
- ^c Theoretical Division, Los Alamos National Laboratory, Los Alamos, NM, 87545, USA
- ^d Weapons and Materials Research Directorate, US Army Research Laboratory, Aberdeen Proving Ground, MD, 21005, USA
- ^e Materials Science and Technology Division, Los Alamos National Laboratory, Los Alamos, NM, 87545, USA
- f Turbocam Energy Solutions, Turbocam International, Dover, NH, 03820, USA

ARTICLE INFO

Keywords: Microstructures Polycrystalline material Crystal plasticity Numerical algorithms Inconel 718

ABSTRACT

In this work, strength and microstructural evolution of superalloy Inconel 718 (IN718) are characterized as a function of the initial microstructure created via direct metal laser melting (DMLM) additive manufacturing (AM) technology along with subsequent hot isostatic pressing (HIP) and heat treatments as well as wrought processing. Stress-strain curves are measured in tension and compression from room temperature to 550 °C and crystallographic texture is characterized using neutron diffraction. Furthermore, a recently developed crystal plasticity model incorporating the effects of precipitates is extended to interpret the temperature dependent deformation behavior of the alloy. The model accounts for solid solution, precipitate shearing, and grain size and shape contributions to initial slip resistance, which evolves with a dislocation density-based hardening law considering latent hardening, while non-Schmid effects are taken into account in the activation stress. Part of the experimental data is used for calibration of the model, while the rest is used for experimental validation of the model. It is shown that the model is capable of modeling the data with accuracy. Based on the comparison of the data and model predictions, it is inferred that the grain structure and texture give rise to plastic anisotropy of the alloy, while its tension-compression asymmetry results from non-Schmid effects and latent hardening.

E-mail address: marko.knezevic@unh.edu (M. Knezevic).

^{*} Corresponding author. University of New Hampshire, Department of Mechanical Engineering, 33 Academic Way, Kingsbury Hall, W119, Durham, NH, 03824, United States.

1. Introduction

Inconel 718 (IN718) superalloy is well known for its high strength, toughness, and corrosion resistance and is widely used for a number of components operating under mechanical and thermal extremes (Barrett et al., 2018; Francis et al., 2014; Knezevic et al., 2012b; Knezevic and Ghorbanpour, 2018; Kuo et al., 2009; Mei et al., 2015; Rao et al., 2003; Slama and Abdellaoui, 2000). Yet the parts for such applications are of complicated shape, requiring careful machining. Due to the high strength and hardness of alloy 718, the cutting tools wear relatively quickly translating into a high cost of machining. Additive manufacturing (AM) is a technology that can print complex shapes from powders, minimizing the need for machining. AM of the alloy and its behavior have recently been extensively studied (Amato et al., 2012; Gribbin et al., 2016).

The alloy has a relatively complex microstructure, featuring several precipitates and carbides in a γ matrix (Antolovich, 2015; Rao et al., 2003; Xiao et al., 2005). These are summarized in Table 1. These precipitates govern the behavior of the alloy. Their volume fraction and distribution depend on processing. For example, the content of δ precipitates was found to be significantly larger in AM IN718 (Gribbin et al., 2019) than wrought processing. Octahedral $\{111\}\langle 1\overline{1}0\rangle$ slip systems accommodate plastic deformation of γ matrix. Additionally, the activity of the six cubic $\{001\}\langle 110\rangle$ glide systems has been reported at the high temperatures associated with wrought processing of the alloy (Ding et al., 2004; Haddou et al., 2004; Österle et al., 2000; Semiatin et al., 2004).

The strengthening results from the γ' and γ'' precipitates, which are shearable by dislocations. After the dislocations cut through them, an anti-phase boundary (APB) in the precipitate is left behind. APB can further contribute to strengthening by increasing the energy of the crystal (Gleiter and Hornbogen, 1968; Huther and Reppich, 1978; Maciejewski et al., 2013). Therefore, knowledge of the values of APB energy would benefit an understanding of precipitate strengthening. For instance, the APB energy for the cubic planes was found to be lower than that for the octahedral planes (Umakoshi et al., 1984), which provided an explanation for why screw dislocations would tend to cross slip onto the {001} planes. The calculated values for APB energies for γ' and γ' precipitates have been presented in our earlier study (Ghorbanpour et al., 2017). In contrast to γ' or γ'' strengtheners, the APB for δ precipitates has not been studied in the past, likely because of size of these precipitates. However, δ precipitates in AM alloy IN718 vary in size substantially and a fraction of them could be sheared (Gribbin et al., 2019), and thus quantification of their APB energy is warranted.

The stress-strain response of the alloy shows a pronounced tension-compression (T-C) asymmetry (Copley and Kear, 1967a, b; Keshavarz and Ghosh, 2015). These have been attributed to the complex microstructural features and the non-Schmid effects at the slip level (Bhattacharyya et al., 2015; Dao and Asaro, 1993; Knezevic and Bhattacharyya, 2017; Schmid and Boas, 1950). Relationships between microstructure, mechanisms, and mechanical behavior have been studied using microstructure-based constitutive laws (Francis et al., 2014; Keshavarz and Ghosh, 2015; Shenoy et al., 2008). These works have focused on room temperature behavior. Considerably less attention has been dedicated to modeling of high temperature plastic behavior. The anisotropic response of γ/γ' superalloy single crystals at 650 °C was examined in (Estevez et al., 1997; Hoinard et al., 1995). The hardening anisotropy was comparable to that of most anisotropic pure face-centered cubic (FCC) metals, likely because the hardening asymmetry on the octahedral slip systems is similar.

In this work, we study the stress-strain behavior of IN718 that has been additively manufactured at elevated temperatures of 450 °C and 550 °C, corresponding to typical service temperatures for this alloy. This work extends the elasto-plastic self-consistent (EPSC) mean-field homogenization, originally developed in (Barrett and Knezevic, 2019; Neil et al., 2010; Turner and Tomé, 1994; Zecevic et al., 2017; Zecevic and Knezevic, 2017, 2019) and recently advanced to P-EPSC for IN718 (Ghorbanpour et al., 2017), to model temperature dependent behavior of IN718. The model incorporates latent hardening, a temperature-dependent initial slip resistance and a temperature-dependent hardening law that explicitly evolves a set of dislocation densities. The initial slip resistance accounts for the effects of grain shape and size and the formation of APB in precipitates as mobile dislocations shearing through them.

The model is calibrated and validated on the comprehensive set of data on IN718 that has been created by AM. We demonstrate its capability to replicate both the texture evolution and stress-strain response to large strains across a broad range of temperatures and the dependence of the mechanical behavior built in different directions. The model suggests that the anisotropy stems primarily from

Table 1
Phases in alloy IN718.

	Phase	Crystal	Space	Composition	Lattice	Lattice Parameters (Å)		References
		structure	group		а	b	с	
Solid solution matrix	γ	Cubic	Fm-3m	Co,Cr,Ni,Fe - Based	3.59	-	-	Murr et al. (2011) Amato et al. (2012) Murr et al. (2012)
Intermetallic	γ'	Cubic	Pm-3m	Ni ₃ (Ti,Al,Nb)	3.58	_	_	Mukherji et al. (2003)
	γ''	Tetragonal	I4/mmm	Ni ₃ Nb	3.62	-	7.41	Murr et al. (2011)
								Amato et al. (2012)
								Murr et al. (2012)
	δ	Orthorhombic	Pmmn	Ni ₃ Nb	4.55	4.25	5.11	Amato et al. (2012)
Topographically close-packed	η	Hexagonal	P63/mmc	Ni ₃ (Ti,Al)	5.10	_	8.30	Evans et al. (2004)
(intermetallic)	Laves	Hexagonal	P63/mmc	(Ni,Cr,Fe)2(Nb,	4.83	_	7.88	Manikandan et al.
				Ti)				(2015)
Carbide	MC	Cubic	Fm-3m	(Nb,Ti)(C,N)	4.46	_	_	Mostafa et al. (2017)
	$M_{23}C_6$	Cubic	Fm-3m	$(Cr,Fe)_{23}C_6$	10.60	-	-	Evans et al. (2004)

Table 2
Alloy IN718 composition in wt%.

Ni	Cr	Nb	Mo	Ti	Mn	Si	Cu	Al	С	S	P	В	Fe
55.5	18.2	5.5	3.3	1.15	0.35	0.35	0.3	0.3	0.08	0.015	0.015	0.006	Bal

the texture and elongated grain structure oriented along the build direction, while asymmetry is due to non-Schmid activation and latent hardening.

2. Material and experiments

2.1. Additive manufacturing

The compression/tension specimens have been fabricated using direct metal laser melting (DMLM) in the EOS M280 machine. The powder produced by gas atomization had an average diameter of 35 μ m, and a range of < 1 μ m to 80 μ m. The chemical composition is given in Table 2, meeting the chemical composition of the IN718 standard. Details pertaining to DMLM are given in (Gribbin et al., 2016). The material was printed in the form of bars and rods, which were subsequently machined into the samples for testing. Three categories of the DMLM IN718 samples are prepared for testing in tension and compression to evaluate the effect of their associate microstructures on strength. The three categories are different orientations with respect to the build direction (BD) and will be labeled as: H-horizontal, D-diagonal at 45°, and V-vertical. Hot isostatic pressing (HIP) treatment was done for a set of samples at 1163 °C for 4 h under 100 MPa. Finally, samples of wrought IN718 were machined from a shaped forging with sample loading direction perpendicular to the axial direction. The samples of every material category were heat treated (HT) after machining according to AMS 5663. The AMS 5663 HT is a solution treatment at 954 °C for 1 h, fan cooling in argon to below 120 °C, and double aging. The double aging involves holding samples at 718 °C for 8 h, followed by furnace cooling at a rate of 50 °C/h to 621 °C, holding at 621 °C for 8 h, and finally air cooling to room temperature.

2.2. Texture and microstructure

Electron backscattered diffraction (EBSD) characterization of grain structure in the three material categories have been presented in (Gribbin et al., 2019). In the present paper, the bulk texture in the samples before and after deformation was measured using neutron diffraction.

2.3. Mechanical testing

Room temperature (RT) tensile data is taken from (Gribbin et al., 2016; Smith et al., 2016), while room temperature compression data for DMLM materials is taken from (Smith et al., 2016). Room temperature compression testing of the DMLM + HIP and wrought samples is performed here for the first time. Consistent with the procedure presented in (Ghorbanpour et al., 2019a, b; Jahedi et al., 2017; Knezevic et al., 2010; Smith et al., 2016), these tests are performed on an Instron Model # 1350 servohydraulic testing machine with DAX software and controller. The machine was equipped with a customized compression fixture consisting of two cylindrical compression dies aligned vertically along the axis of the actuator. Compliance of the testing setup was measured by compressing the dies without a specimen to correct the raw data before computing the true stress—true strain curves. The samples were compressed to a true strain of approximately 0.5 (i.e. the tests are interrupted before sample fracturing). Three samples are tested per category.

Tensile testing at two different test temperatures ($450\,^{\circ}$ C and $550\,^{\circ}$ C) was carried out on subsized, flat and dog-bone shaped specimens with a nominal gage section of $12.7x3.0x1.2\,\text{mm}$. First, the gage section of these DMLM IN718 specimens was machined down, by the electrical discharge machining (EDM), to half of their original length to reduce the force required to break the specimens, and to facilitate high temperature friction gripping without slippage. All the machined specimens were polished up to 1500 grit SiC paper to remove surface oxidation (if any) and damage caused by the EDM. They were then cleaned in ultrasonic vibrator using water. An MTS 810 servo-hydraulic universal testing machine (capacity: $250\,\text{kN}$) equipped with a clamshell furnace (MTS 657.02, capacity $1600\,^{\circ}$ C) was used to conduct the tests in the air at $450\,^{\circ}$ C and $550\,^{\circ}$ C, with $\pm 1\,^{\circ}$ C accuracy. The specimens were heated to the target temperature at load-control mode and held for 30 min before shifting to displacement control for testing at a displacement rate of 0.75 mm/min, or a strain rate $\approx 10^{-3}$ /s. A high temperature extensometer (MTS 632.53E-11, range: $\pm 20\%$ of 25.4 mm), with ceramic arms extending into the furnace, was used to measure the specimen displacement. The load and displacement of the actuator were also recorded for verification. The samples were deformed to failure. Tensile properties were determined according to the ASTM test standard E8M-13 (2013).

Simple compression tests were conducted on cylindrical IN718 specimens, EDMed down to 4 mm diameter from their original 6 mm diameter in order to reduce the load required to deform the specimens at high temperature. However, to maintain consistency with the room temperature test (Smith et al., 2016), the length to diameter ratio was kept 1.2. Both surfaces of the specimens are polished using 1500 grit SiC paper.

All compression tests were performed on the same MTS 810 machine, and using the same furnace and extensometer as the high-temperature tensile tests. However, the machine was equipped with a customized compression fixture consisting of two cylindrical

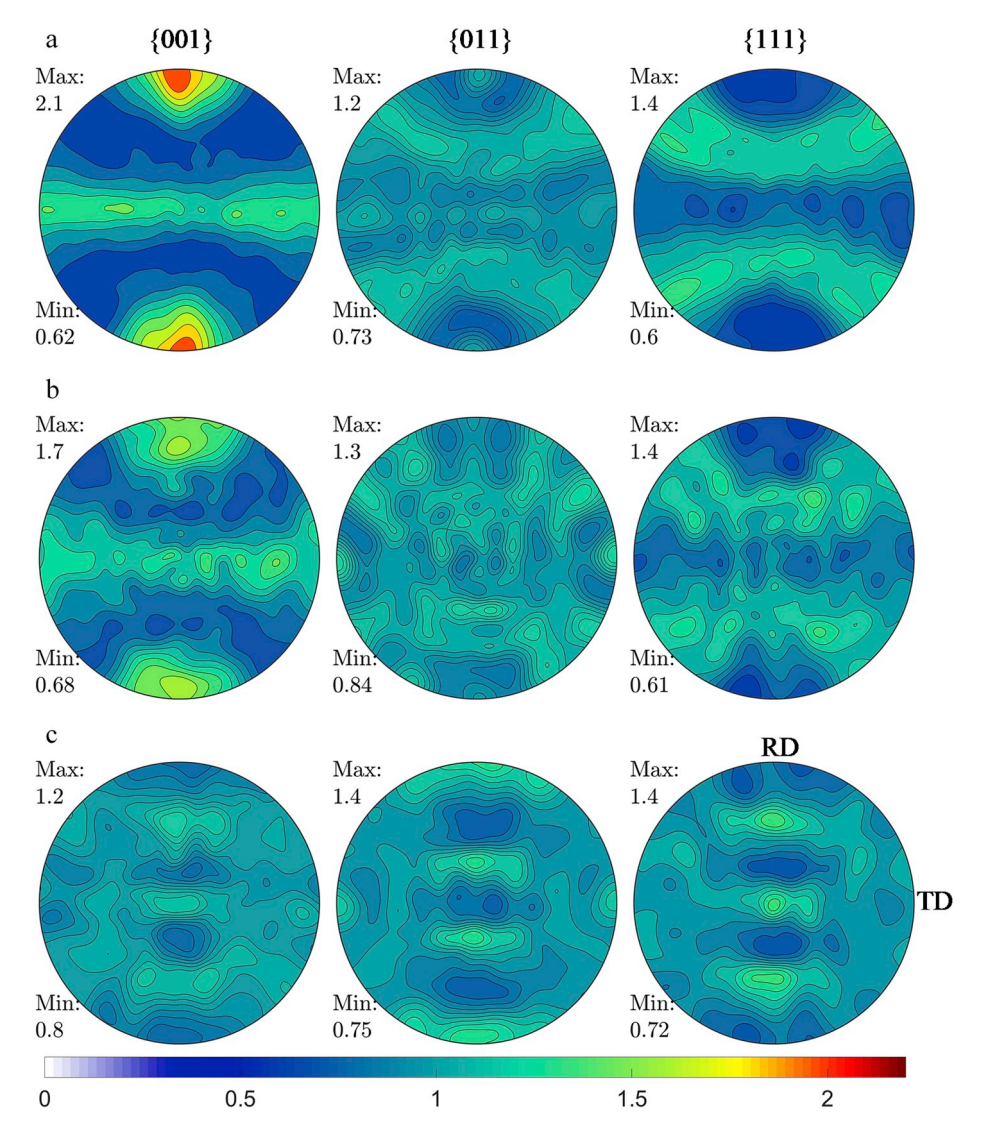


Fig. 1. Stereographic pole figures as measured using the neutron diffraction technique showing the initial crystallographic texture in the samples of IN718: (a) DMLM, (b) DMLM + HIP, and (c) wrought. BD is vertical for (a) and (b).

compression dies aligned vertically along the axis of the actuator. The compression dies are made of Inconel with smooth, flat surfaces. Tungsten carbide (WC) bearing blocks (5 mm thick, 20 mm diameter), also flat-surfaced, were used at both sides of the dies to protect the face of the Inconel dies and to help transmit the axial load. Boron nitride spray-II was used to minimize the effects of contact friction between the faces of the specimen and the upper and lower compression dies and blocks. All the dies and the blocks were aligned before tests and found parallel to the loading axis after tests.

The samples were compressed to a true strain of approximately -0.25 to -0.4. The maximum strain is determined by the maximum compressive load that the WC can bear ($25 \, \text{kN} - 30 \, \text{kN}$) before shattering at that temperature. The tests were performed at a strain rate of 10^{-3} /s in the air at $550 \,^{\circ}$ C. Three samples were deformed per category to ensure the reputability and accuracy of the measured data. Compression test loads and displacements were measured in accordance with the ASTM E-09-09 and E-209 standards (2018a; 2018b).

3. Experimental results

This section presents results of mechanical testing and texture characterization for alloy IN718.

3.1. Texture and microstructure

The initial grain structure in all samples (DMLM, DMLM + HIP, and wrought) were characterized previously in (Gribbin et al.,

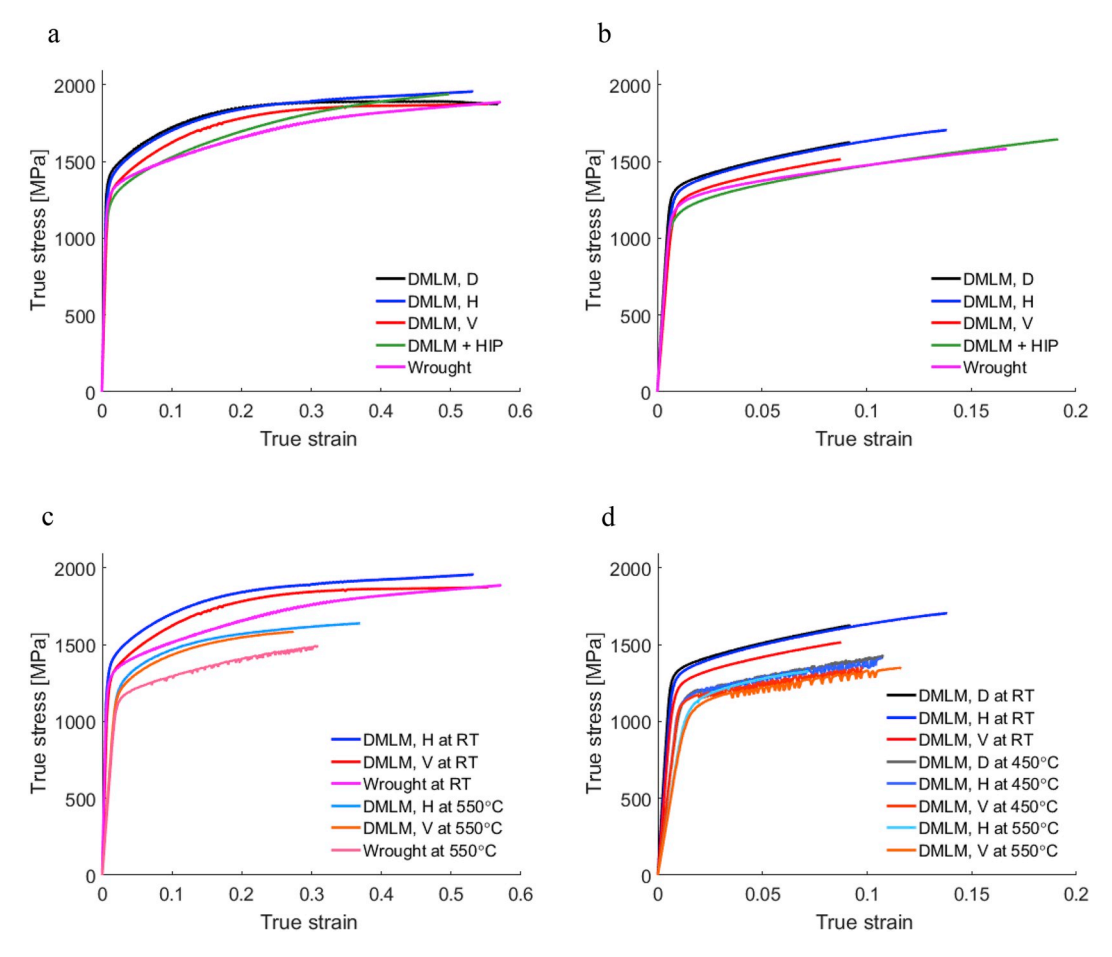


Fig. 2. Simple tension and compression responses of IN718 as a function of sample orientation and temperature measured under 0.001/s strain rate: (a) compression: DMLM along D, H, and V, DMLM + HIP, and wrought at RT, (b) tension: DMLM along D, H, and V, DMLM + HIP, and wrought at RT, (c) compression: DMLM along V and H, and wrought at RT, DMLM along V and H, and wrought at 550 °C, (d) tension: DMLM along V, D, and H at RT, DMLM along V, D, and H at 450 °C, DMLM along V, and H at 550 °C. The samples tested in tension went to fracture, while those tested in compression were interrupted before fracture.

2019). It was found that the DMLM material exhibits a strongly elongated grain structure along the deposition direction (average major and minor axis of 130 μ m and 25 μ m, respectively), while the aspect ratio is significantly reduced in the DMLM + HIP material but grains are much coarser (average major and minor axis of 280 μ m and 80 μ m, respectively). Incoherent annealing twins are introduced in the microstructure by HIP treatment. Wrought material exhibits an equiaxed grain structure of approximately 105 μ m and a large fraction of the coherent twin boundaries. Porosity content was also studied in the earlier work (Smith et al., 2016). The content of porosity in the DMLM material was found to be approximately 0.18% with 0% in DMLM + HIP and wrought.

It was found that the δ precipitates in the DMLM material were intragranular with some present along the grain boundaries (GBs) (Gribbin et al., 2019). In contrast, the δ precipitates in the DMLM + HIP and wrought materials were primarily along the GBs. The high fraction of intragranular δ precipitates in the DMLM sample was attributed to heterogeneity in the solidification microstructure that occurred during the DMLM process, whereas localized inter-dendritic regions can have relatively high concentrations of Nb and Ni (Lass et al., 2017). GB δ precipitates in DMLM + HIP and wrought samples were much larger than those in the DMLM. The DMLM + HIP and wrought samples also contain carbides. Existence of δ precipitates of variable size in the DMLM material suggests that both shearing and looping hardening mechanisms will be activated during their interaction with mobile dislocations. Due to their size in IN718 both γ '' and γ' are shearable. In addition to shearing of γ '' and γ ', the shearing contribution from the δ phase is also considered but the contribution is very small. Importantly, we have been able to fit the initial slip resistance without considering any looping, which suggests that looping has a minimal effect in alloy IN718. The content of δ precipitates was 7.9% in DMLM, while only 0.7% in DMLM + HIP and 0.8% in wrought (Ferreri et al., 2019).

Crystallographic texture has also been characterized using EBSD (Smith et al., 2016). However, the micro technique is not well suited to do so, especially for coarse grained materials. In the present work, the textures have been characterized using neutron diffraction (Fig. 1). As shown, a moderately strong <100> fiber along the deposition direction is found for DMLM. As a result of the preferential grain structure and texture, the mechanical response will vary among the V, D, and H samples. Texture in the DMLM + HIP

Table 3
Yield stress estimates at 0.2% offset strain in tension and compression (expressed in [MPa]). The values are average of 2 or 3 tests.

	DMLM, V	DMLM, D	DMLM, H	DMLM + HIP	Wrought
Tension at RT	1215	1305	1290	1105	1170
Compression at RT	1255	1370	1345	1125	1205
Tension at 450 °C	1110	1130	1125	_	-
Tension at 550 °C	1015	_	1045	_	-
Compression at 550 °C	1135	-	1160	_	1100

material is even weaker, which is a consequence of static recrystallization and grain growth. Texture in the wrought material is a consequence of the ring rolling process. Weak to moderately strong textures in the samples will likely have a secondary effect on the plastic behavior of these materials.

3.2. Stress-strain response

Fig. 2 shows the measured true stress-true strain data at room temperature and two elevated temperatures 450 °C and 550 °C. The DMLM samples are stronger in tension and compression than DMLM + HIP and wrought materials. However, wrought and DMLM + HIP samples show more elongation to fracture. Initial microstructures of the samples govern such behavior. The DMLM material contains some porosity limiting its elongation to fracture. The DMLM material exhibits much smaller grains than wrought and DMLM + HIP, making it stronger, as explained below. The difference in the behavior between the DMLM V, H, and D samples is driven by the grain morphology and texture. As explained earlier, the HIP treatment changes the structure to a coarse-grained one and randomizes the texture. The treatment also dissolves the precipitates, including the δ precipitates, and rebuilds them in different amounts. These δ precipitates are not dissolved during the subsequent heat treatment per AMS 5663. Thus, the material is comparatively softer and more ductile than the DMLM material without HIPing. The wrought material also has a coarser grain structure making it weaker than the DMLM material. Among the room temperature tests on the DMLM material, the V sample shows relatively lower strength than the H and D counterparts, both in tension and compression (Fig. 2). This trend also persists at high temperatures, although the difference in strengths among the V, H, and D samples has slightly reduced. Since presented in the form of true stress-true strain, the provided elevated temperature tensile data is up to the maximum load point, meaning that the softening portion of the curves is not shown. The 0.2% yield strength (YS) slightly decreases with increasing temperature from RT to 550 °C, but are still comparable (especially for DMLM D and H) to the room temperature HIPed and wrought alloy (Table 3). However, DMLM samples in all three build directions exhibited some T-C asymmetry, which will be shown using modeling results.

Some of the high temperature stress-strain curves for tensile test shown in Fig. 2 reveal dynamic strain aging (DSA) or serration, which is common in some metals, including Ni-based alloys that generally occurs during plastic deformation within a specific temperature range and strain rate (Beese et al., 2018; Cai et al., 2017; Hayes and Hayes, 1982; Maj et al., 2014; Mannan, 1993). In our case, type-C serration was seen of tested specimens for all three DMLM samples at 450 °C, and only for DMLM-V sample at 550 °C in tension, although their spacing and stress-amplitude vary (see Fig. 2). A critical strain is also required to initiate the serrated response, which is ~0.02 at 450 °C for all three DMLD specimens, ~0.035 for DMDL-V at 550 °C. It is widely accepted that the DSA occurs due to the interaction between diffusing solute atoms and mobile dislocations that are blocked by these solute atoms and strengthen materials. When the stress reaches a critical value, these mobile dislocations are released and thereby a lower stress is needed for deformation, resulting serration in the stress-strain curve (Beese et al., 2018; Cai et al., 2017; Maj et al., 2014). We note that the compression test at 550 °C for all three DMLM specimens did not show such a serrated response or DSA. On the contrary, the IN718-wrought (forged) sample exhibited serration at the same temperature in compression. This finding is consistent with (Beese et al., 2018), who observed DSA for conventionally processed Inconel 625, whereas an absence of DSA for the AM-processed counterpart during compression at 600 °C. The presence of coarser precipitates, especially carbides, at grain boundaries is the main reasons for serration of wrought IN718 (Beese et al., 2018; Mannan, 1993; Weaver and Hale, 2001). The DMLM processed IN718 does not contain coarser carbide and delta phases at grain boundaries but much more dispersed intra-granular delta phases (Gribbin et al., 2019). The dislocation arrest theory (proposed by (Sleeswyk, 1958)) and supported by many subsequent works (Beese et al., 2018; Hayes and Hayes, 1984)) assumes that solute atmospheres (carbon atoms) form on forest dislocations. At room/low temperature, solute atoms are immobile within the lattice, however, they become mobile along with dislocations at higher temperature. As mobile dislocations glide under applied loading, they encounter obstacles like immobile forest dislocation surrounded by solute ambience. The obstacles could temporarily or permanently arrest mobile dislocations. If temporarily, during the waiting time, solute atoms drain from forest dislocations to mobile dislocations via pipe diffusion. This accumulation of solute atoms in mobile dislocations further strengthens the obstacles that raise the critical stress needed to overcome these obstacles. When the applied flow stress exceeds the critical stress, these mobile dislocations quickly move to the next obstacles (with increased strain and relaxed stress). The process repeats leading to the serration. For DMLM processed IN718, these mobile dislocations are obstructed by the finely distributed precipitates at the grain interior whit high dispersion hardening effect. The precipitates can react with carbon and act as sinks for solute atoms; therefore, draining carbon from the mobile dislocation rather than forming obstacles. However, for wrought IN718, the large carbides and delta phases are coarsely distributed, mostly along the grain boundaries, so, the probability for arresting mobile dislocations is low because of low dispersion hardening effect. This allows mobile dislocations to move freely until arrest at the forest dislocations, and dislocation pipe diffusion mechanism dominates during waiting time, resulting in serration during deformation. Details of the dislocation arrest theory can be

found in (Beese et al., 2018; Hayes and Hayes, 1984; Sleeswyk, 1958). Grain size and texture also play their role on DSA behavior (Beese et al., 2018; Mannan, 1993). It is also well established that the negative strain rate sensitivity of the flow stress is correlated with DSA phenomena (Beese et al., 2018; Hayes and Hayes, 1984; Mannan, 1993).

4. Modeling framework

The recently developed P-EPSC (Ghorbanpour et al., 2017) is advanced here into a temperature dependent constitutive law for IN718, by applying it to model the behavior of the alloy across a temperature range from room to 550 °C. The model integrates a dislocation density-based hardening law. While precipitates are not modeled explicitly because of their size, the model takes into account the effect of the APB formation in γ' , γ'' , and δ precipitates into the slip resistance. Finally, the model considers latent hardening and non-Schmid activation stresses. In our description, we use "·" to denote a dot product and " \otimes " to denote a tensor product.

The EPSC model represents a polycrystal as an aggregate of grains with a distinct crystallographic orientation and volume fraction. Each grain is modeled as an elasto-plastic ellipsoid inclusion in a homogeneous medium. The constitutive response of the polycrystalline aggregate is assumed to follow a linear relationship given by:

$$\hat{\mathbf{\sigma}} = \mathbf{L}\dot{\mathbf{\varepsilon}}$$
 (1)

where L is the instantaneous elasto-plastic stiffness tensor of the polycrystal, $\hat{\sigma}$ is the macroscopic Jaumann stress rate, and $\dot{\epsilon}$ the strain rate. The self-consistent scheme solves for L iteratively (Turner and Tomé, 1994; Zecevic et al., 2017, 2019; Zecevic and Knezevic, 2017) until equilibrium and strain compatibility are satisfied (Eshelby, 1957). The polycrystalline $\dot{\epsilon}$ is related to the strain rate of the individual crystals $\dot{\epsilon}^c$ according to

$$\dot{\varepsilon}^c = A^c \dot{\varepsilon}$$
 (2)

where $\mathbf{A}^c = (\mathbf{L}^c + \mathbf{L}^{c^*})^{-1}(\mathbf{L}^{c^*} + \mathbf{L})$ is the localization tensor for the ellipsoidal inclusion c, \mathbf{L}^c is its instantaneous elasto-plastic stiffness tensor and $\mathbf{L}^{c^*} = \mathbf{L}(\mathbf{S}^{c-1} - \mathbf{I})$ is its effective stiffness tensor. Note that the latter contains the symmetric Eshelby tensor \mathbf{S}^c . I is the fourth rank identity matrix. The tensor \mathbf{L}^{c^*} relates the grain stress and total strain rate to the polycrystalline (i.e., homogeneous medium) stress and total strain rate through an interaction equation, given by

$$(\widehat{\boldsymbol{\sigma}}^c - \widehat{\boldsymbol{\sigma}}) = -\mathbf{L}^{c^*}(\dot{\boldsymbol{\epsilon}}^c - \dot{\boldsymbol{\epsilon}}),$$

In the self-consistent scheme, the polycrystal stress and strain rate are enforced to be equal to the volume average of the stress and strain rate in all grains:

$$\widehat{\mathbf{\sigma}} = \left\langle \widehat{\mathbf{\sigma}}^c \right\rangle$$
 (3)

and

$$\dot{\mathbf{c}} = \left\langle \dot{\mathbf{c}}^c \right\rangle \tag{4}$$

The above conditions lead to the following expression for L:

$$L = \langle L^c A^c \rangle \langle A^c \rangle^{-1} \tag{5}$$

Finally the macroscopic stress is updated using the following relationship between the Cauchy stress rate and Jaumann rate $\dot{\sigma} = \hat{\sigma} + \langle \mathbf{W}^c \mathbf{\sigma}^c \rangle - \langle \mathbf{W}^c \mathbf{G}^c \rangle - \langle \mathbf{W}^$

For an individual grain, the constitutive relationship is:

$$\widehat{\mathbf{\sigma}}^{c} = \mathbf{C}^{c} \left(\dot{\mathbf{\epsilon}}^{c} - \sum_{\mathbf{m}} \mathbf{m}^{c,s} \dot{\mathbf{\gamma}}^{c,s} \right) - \mathbf{\sigma}^{c} tr(\dot{\mathbf{\epsilon}}^{c})$$
(6)

where the grain Jaumann stress rate is $\hat{\mathbf{g}}^c$, the grain strain rate is $\dot{\mathbf{e}}^c$, the grain stiffness tensor is \mathbf{C}^c and the grain plastic strain rate is $\sum_s \mathbf{m}^{c,s} \dot{\gamma}^{c,s}$. The latter is given by the sum of the product of the shear strain rates, $\dot{\gamma}^{c,s}$, from each slip system, s, and the tensor $\mathbf{m}^{c,s} = 0.5(\mathbf{b}^{c,s} \otimes \mathbf{n}^{c,s} + \mathbf{n}^{c,s} \otimes \mathbf{b}^{c,s})$, which is the symmetric part of the Schmid tensor for slip system s. The Schmid tensor is calculated as the tensor product of $\mathbf{b}^{c,s}$ and $\mathbf{n}^{c,s}$, the orthonormal unit vectors representing the slip direction and slip plane normal, respectively. Since the grain orientation can change during deformation, the elastic stiffness and Schmid tensors are updated at the beginning of each deformation increment.

Due to the core structure of dislocations in Ni-based superalloys, non-Schmid effects can be important. Non-Schmid effects are

included in the crystal level constitutive law via the introduction of a non-Schmid tensor $\mathbf{m}_{ns}^{c,s}$. To define $\mathbf{m}_{ns}^{c,s}$, we consider five non-glide stress components: the two shear stresses $\mathbf{t}^{c,s} \otimes \mathbf{b}^{c,s}$ and $\mathbf{t}^{c,s} \otimes \mathbf{n}^{c,s}$, acting normal to the Burgers vector and the three normal stresses $\mathbf{n}^{c,s} \otimes \mathbf{n}^{c,s}$, $\mathbf{n}^{c,s} \otimes \mathbf{t}^{c,s} \otimes \mathbf{t}^{c,s}$, and $\mathbf{b}^{c,s} \otimes \mathbf{b}^{c,s}$. These components are related to the non-Schmid tensor via (Dao and Asaro, 1993; Knezevic et al., 2014a, 2015a; Lim et al., 2013; Savage et al., 2017, 2018):

$$\mathbf{m}_{c,s}^{(s)} = c_1(\mathbf{t}^{e,s} \otimes \mathbf{b}^{e,s}) + c_2(\mathbf{t}^{e,s} \otimes \mathbf{n}^{e,s}) + c_3(\mathbf{n}^{e,s} \otimes \mathbf{n}^{e,s}) + c_4(\mathbf{t}^{e,s} \otimes \mathbf{t}^{e,s}) - (c + c_4)(\mathbf{b}^{e,s} \otimes \mathbf{b}^{e,s})$$

$$(7)$$

The non-Schmid tensor is added to the Schmid tensor to give the total Schmid tensor where $\mathbf{m}_{tot}^{c,s} = \mathbf{m}^{c,s} + \mathbf{m}_{ns}^{c,s}$ to provide the stress used to activated slip:

$$\mathbf{m}^{c,s} \cdot \mathbf{\sigma}^c + \mathbf{m}^{c,s} \cdot \mathbf{\sigma}^c = \mathbf{m}^{c,s} \cdot \mathbf{\sigma}^c \tag{8}$$

In Eq. (7), c_i is the weighting coefficient for the non-Schmid effect i. Only four coefficients are needed since only four are independent under incompressible flow.

The relationship between the evolution of slip resistance, $i_c^{c,s}$, and the rates of slip on other slip systems is given by (Zecevic and Knezevic, 2015, 2018a):

$$\dot{\tau}_c^{c,s} = \sum_{s'} h^{ss'} \dot{\gamma}^{c,s'} \tag{9}$$

where h^{ss} is the hardening matrix. Expressions for h^{ss} are given in (Zecevic and Knezevic, 2015).

Combining relations (6) and (9) with $\mathbf{m}_{tot}^{c,s} \cdot \hat{\mathbf{g}}^c = \dot{\tau}_c^{c,s}$ gives a set of linear equations for the shear rates:

$$\mathbf{m}_{tot}^{c,s} \cdot \left(\mathbf{C}^c \left(\dot{\mathbf{c}}^c - \sum_{s} \mathbf{m}^{c,s} \dot{\gamma}^{c,s} \right) - \mathbf{\sigma}^c tr(\dot{\mathbf{c}}^c) \right) = \sum_{s} h^{ss} \dot{\gamma}^{c,s}$$
(10)

These shear rates are related to the strain rate in crystal following

$$\dot{\boldsymbol{\gamma}}^{c,s} = \left(\sum_{s'} \left(\boldsymbol{X}^{ss'}\right)^{-1} \mathbf{m}_{tot}^{c,s'} \left(\mathbf{C}^c - \boldsymbol{\sigma}^c \otimes \mathbf{i}\right)\right) \cdot \dot{\boldsymbol{\varepsilon}}^c \tag{11}$$

where

$$X^{ss} = h^{ss} + \mathbf{C}^c \cdot \mathbf{m}^{c,s} \otimes \mathbf{m}^{c,s}$$
 (12)

Given the above, the modulus L^c that relates the grain strain rate and Jaumann rate according to

$$\widehat{\mathbf{\sigma}}^c = \mathbf{L}^c \widehat{\mathbf{\epsilon}}^c$$
 (13)

can be calculated

$$\mathbf{L}^{c} = \mathbf{C}^{c} - \mathbf{C}^{c} \sum_{s} \mathbf{m}^{c,s} \otimes \left(\sum_{s} (X^{ss'})^{-1} \mathbf{m}_{tot}^{c,s'} (\mathbf{C}^{c} - \mathbf{\sigma}^{c} \otimes \mathbf{i}) \right) - \mathbf{\sigma}^{c} \otimes \mathbf{i}$$
(14)

Finally, to update the texture, we calculate the lattice rotation rate tensor, \mathbf{W}^c , according to

$$\mathbf{W}^{c} = \mathbf{W}^{app} + \mathbf{\Pi}^{c} - \mathbf{W}^{p,c} \tag{15}$$

where \mathbf{W}^{app} is the applied rotation rate, $\mathbf{\Pi}^c$ is the antisymmetric part of the Eshelby tensor (Lebensohn and Tomé, 1993), and $\mathbf{W}^{p,c}$ is the plastic rotation rate. The latter is related to the slip system slip rates according to:

$$\mathbf{W}^{p,c} = \sum_{s} \mathbf{q}^{c,s} \dot{\gamma}^{c,s} \tag{16}$$

where $\mathbf{q}^{c,s} = 0.5(\mathbf{b}^{c,s} \otimes \mathbf{n}^{c,s} - \mathbf{n}^{c,s} \otimes \mathbf{b}^{c,s})$.

4.1. First-principles calculations of APB energy for the delta phase in IN718

In prior work, the values of the APB energy within the two γ' and γ'' precipitates were calculated using density functional theory (DFT) (Ghorbanpour et al., 2017). In this work, we additionally calculate the APB energy for the δ phase. The APB energy values are used in the initial slip resistance equations described in the previous section.

To calculate the generalizes stacking fault energy (GSFE) in the delta phase of Ni_3Nb , we performed DFT calculations using the Vienna Ab initio Simulation Package (VASP) code (Kresse and Furthmüller, 1996; Kresse and Hafner, 1994). For exchange correlation functional in DFT, we used generalized gradient approximation (GGA) with the Perdew-Becke-Ernzerhof (PBE) parametrization (Perdew et al., 1996) and Projector-Augmented Wave (PAW) pseudopotentials for the interaction between valence electrons and ionic cores (Blöchl, 1994; Kresse and Joubert, 1999). The numbers of valence electrons are 10 and 13 for the Ni and Nb pseudopotentials, respectively. For the calculations of the lattice constants of the cubic primitive unit cell, we used a $19 \times 19 \times 19$ Γ -centered Monkhorst

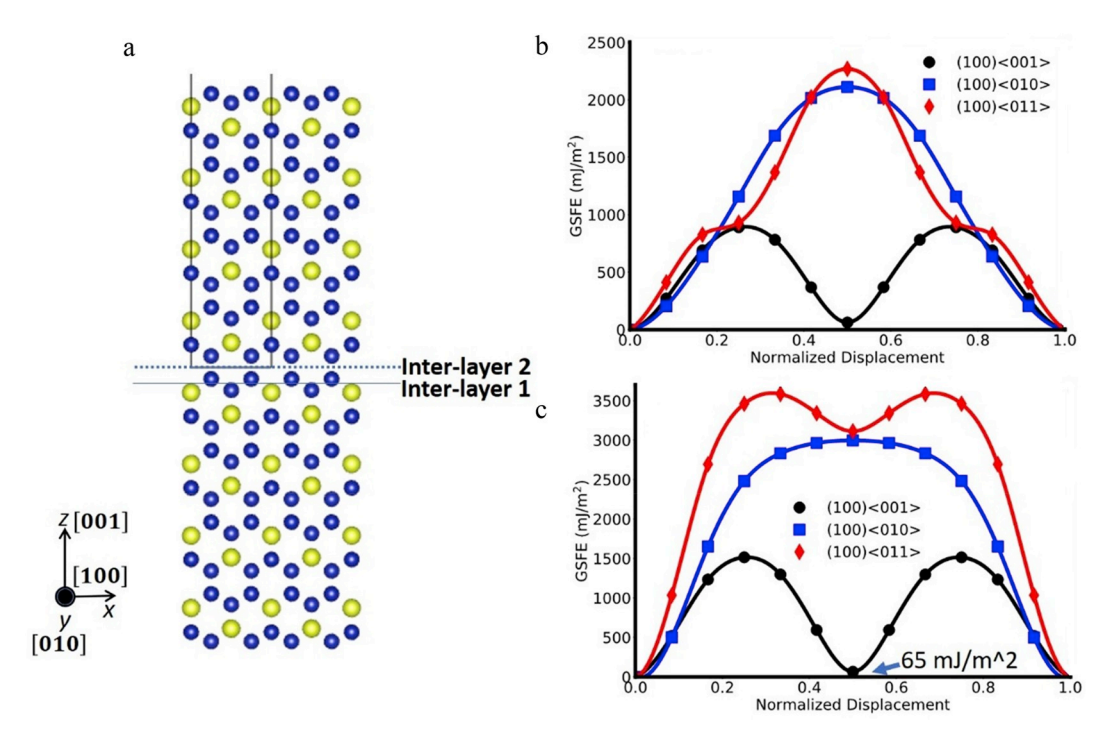


Fig. 3. Generalizes stacking fault energy (GSFE) curves along three directions on (100) plane for Ni₃Nb in the δ phase. Nb atoms are shown in yellow and Ni atoms are shown in blue. (For interpretation of the references to colour in this figure legend, the reader is referred to the Web version of this article.)

Pack k-point to integrate the Brillouin Zone. We used a plane wave energy cutoff of $400\,\mathrm{eV}$, and optimized the atomic structure until the force on each atom is smaller than $0.01\,\mathrm{eV/\mathring{A}}$.

The crystal structure of the delta phase is orthorhombic. The calculated lattice constants for the orthorhombic structure (space group #59) are given in Table 1. To calculate the GSFE curves on (100) plane in Ni_3Nb , we take a periodic supercell consisting of 64 atoms (48 Ni and 16 Nb atoms) as shown in Fig. 3a. Supercell consists of a 15 A thick vacuum layer along the direction normal to slip plane. As shown in Fig. 3a, there are two interlayer distances (0.72 Å and 1.44 Å) along normal to (100) plane. Fig. 3b and c shows the calculated GSFE curves for the interlayer 2 (separation 1.44 Å) and interlayer 1 (separation 0.72 Å) along three directions respectively. The calculated antiphase boundary (APB) energy on the (100) plane is 65 mJ/m².

4.2. Initial resistance to slip

Initial slip resistance is expressed as

$$\tau_0^s = \tau_{0,ss} + \tau_{0,HP}^s + \tau_{0,shear} \tag{17}$$

The contributing terms to the slip resistance are the solid solution strengthening, the Hall-Petch-like barrier effect, and precipitates shearing effect.

The first term is given by

$$\tau_{0,ss} = \frac{1}{M} \sum_{i} \frac{d\sigma}{d\sqrt{g_i}} \sqrt{g_i}$$
 (18)

where M is the Taylor factor, g is the atomic fraction, and $\frac{d\sigma}{d\sqrt{g_i}}$ is the strengthening coefficient of the solute elements in IN718, which are taken from (Roth et al., 1997). Using these values in Eq. (18) along with M for the measured texture, the solid solution strengthening contribution is 263.2 MPa.

The second term is

$$\tau_{0,HP}^{s} = \frac{H \,\mu_{\text{IN}718} \,\sqrt{b}}{\sqrt{d_{mfp}^{s}}} \tag{19}$$

with

Table 4 Data used for the calculation of $\tau_{0.shear}$ using Eq. (21).

	-,	-			
	APB $\left[\frac{mJ}{m^2}\right]$	μ [GPa]	b [nm] $rac{a}{2}\langle 110 angle$	f [%]	<i>r</i> [nm]
γ,	207	78.2	0.254912	13.2	12.5
γ',	378	72.6	0.256255	2.9	5.85
δ	65	84.3	0.3217	1	10

$$d_{mfp}^{s} = \frac{2}{\sqrt{\left(\frac{\hat{b}_{x}^{s}}{a}\right)^{2} + \left(\frac{\hat{b}_{y}^{s}}{b}\right)^{2} + \left(\frac{\hat{b}_{z}^{s}}{c}\right)^{2}}}$$
(20)

where H, b, d_{mfp}^s , and μ_{IN718} are the Hall-Petch coefficient per slip mode, the Burgers vector for the <110> dislocations ($b=2.492\ 10^{-10}\ m$), the mean free path for a given slip system s, and the shear modulus of the alloy, respectively. Component, \hat{b}_x^s , \hat{b}_y^s , \hat{b}_z^s , represent a unit vector in the Burgers direction expressed in a frame of the ellipsoid of size a, b, and c. The value calculated using Eq. (19) averaged over many grains is 67.9 MPa.

The remaining term is (Courtney, 1990; Maciejewski et al., 2013)

$$\tau_{0,shear} = 0.7\mu_{\gamma} \left(\frac{\mathsf{APB}_{\gamma}}{\mu_{\gamma} b_{\gamma}}\right)^{\frac{3}{2}} \left(\frac{f_{\gamma} \bar{r}_{\gamma}}{b_{\gamma}}\right)^{\frac{1}{2}} + 0.7\mu_{\gamma} \left(\frac{\mathsf{APB}_{\gamma}}{\mu_{\gamma} b_{\gamma}}\right)^{\frac{3}{2}} \left(\frac{f_{\gamma} \bar{r}_{\gamma}}{b_{\gamma}}\right)^{\frac{1}{2}} + 0.7\mu_{\delta} \left(\frac{\mathsf{APB}_{\delta}}{\mu_{\delta} b_{\delta}}\right)^{\frac{3}{2}} \left(\frac{f_{\delta} \bar{r}_{\delta}}{b_{\delta}}\right)^{\frac{1}{2}}$$

$$(21)$$

where f is the volume fraction of the precipitate and \bar{r} is the average radius of the precipitates. APB values for γ' and γ'' have been provided in (Ghorbanpour et al., 2017). In this work, we provide the value for δ based on the DFT calculations. As noted above, not all δ precipitates are shearable. Only a small fraction of 1% is assumed shearable. Table 4 presents the input values for Eq. (21). The estimated value is 267.2 MPa.

The initial slip resistance depends on temperature and the values calculated above use input that are applicable to RT. Note, the RT value was obtained with no calibration constants. With measured material response at elevated temperatures, we have the opportunity to characterize this temperature dependence in initial slip resistance. In doing so, we assume that the net value of the resistance considering all contributions will decrease with increases in temperature from room temperature. Individually, the first term in the equation for the initial slip resistance represents the resistance from lattice friction and it is assumed that the increase in lattice vibrations with increase in temperature results in a reduction in this value as a result of weaker atomic bond strength at high temperatures. The second term decrease as well since it aids slip transfer across the grain boundaries. The third term also depends on the temperature through the temperature dependence of APB energy and the shear modulus, which decrease with increases in temperature (Li et al., 2019). In summary, we do not calculate the temperature-dependent APB energy and the shear modulus but establish the temperature-dependent initial slip resistance by fitting the mechanical data.

4.3. Evolution of slip resistance

In this model, we allow for the slip resistance on individual slip systems to evolve with strain, temperature, and strain rate. The slip resistance is defined as (Ardeljan et al., 2014, 2015, 2016, 2017; Ardeljan and Knezevic, 2018; Jahedi et al., 2015; Knezevic et al., 2012a, 2013, 2015b, 2016):

$$\tau_s^c = \tau_0 + \tau_{forest}^s + \tau_{debris} \tag{22}$$

where, τ_{forest}^s is the resistance from the forest of dislocations and τ_{debris} is the resistance from residual dislocation debris from incomplete recovery reactions. The τ_{forest}^s evolves according to (Kitayama et al., 2013):

$$\tau_{forest}^{s} = b\chi\mu_{\text{IN718}} \sqrt{\sum_{s'} L_{ss'}^{s'} \rho_{tot}^{s'}}$$
 (23)

where, $\chi=0.9$ is a dislocation interaction constant, $\mu_{\rm IN718}^{\alpha}$ is the shear modulus in the slip system coordinate system, $\rho_{\rm tot}^{s}$ is the accumulated forest dislocation density for sth slip system and $L^{\rm ss'}$ is a latent hardening interaction matrix explicitly defined in (Ghorbanpour et al., 2017).

The τ_{debris} is related to the density of dislocations stored as debris ρ_{deb} using the extended Taylor law (Madec et al., 2003):

$$\tau_{debris}^{a} = k_{deb}\mu_{\text{IN718}} b\sqrt{\rho_{deb}} log\left(\frac{1}{b\sqrt{\rho_{deb}}}\right)$$
 (24)

where $k_{deb} = 0.086$ is a material independent constant that recovers the Taylor law i.e., Eq. (24) for low values of dislocation density. The rate of stored dislocation density with strain is governed by a competition between the rate of trapping and the rate of recovery.

Table 5 Hardening law constants calibrated as functions of temperature in [K]. T_{ref} is room temperature, 298 K.

$ au_0(T)$ [MPa]	D(T) [MPa]	g	$k_1 \ [m^{-1}]$	q	Н
637.9–37.9*exp((<i>T-T_{ref}</i>)/261.1)	$468.2 + 4.4 \exp(T/150.9)$	0.04	3.2e+8	4.0	0.31

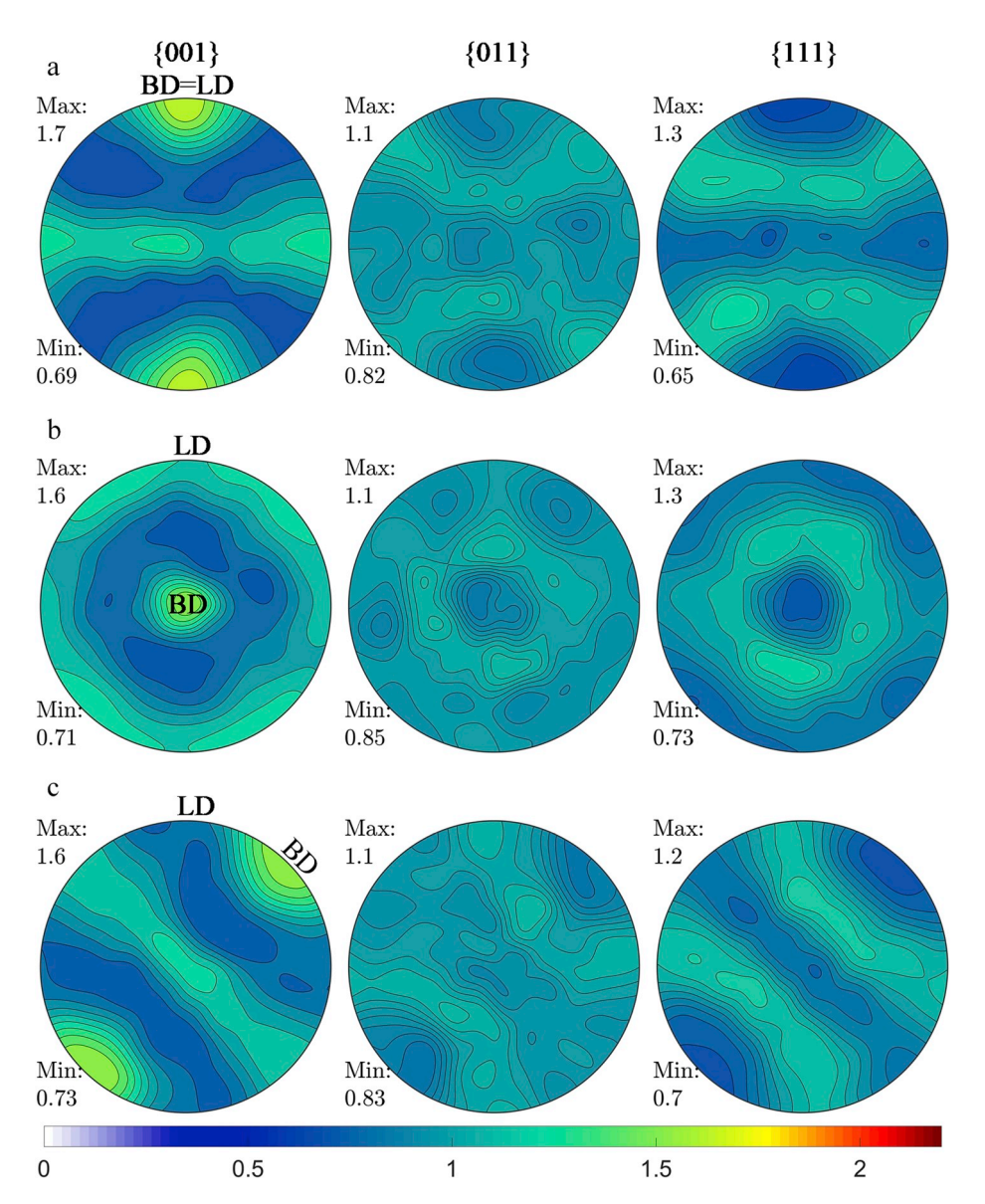


Fig. 4. Stereographic pole figures visualizing texture in the DMLM samples with respect to the loading direction (LD). The texture was constructed from the neutron diffraction measurements (Fig. 1a) and represented with 5000 orientations, which are used in the crystal plasticity modeling.

$$\frac{\partial \rho^s_{tot}}{\partial r^s} = k_1 \sqrt{\rho^s_{tot}} - k_2(\dot{\epsilon}, T) \rho^s_{tot}$$
(25)

The rate coefficient of trapping k_1 is assumed to be insensitive to temperature and strain rate. However, the rate coefficient of recovery k_2 is calculated using:

$$\frac{k_2}{k_1} = \frac{\chi b}{g} \left(1 - \frac{k_B T}{D(b)^3} ln \left(\frac{\dot{\varepsilon}}{\dot{\varepsilon}_0} \right) \right) \tag{26}$$

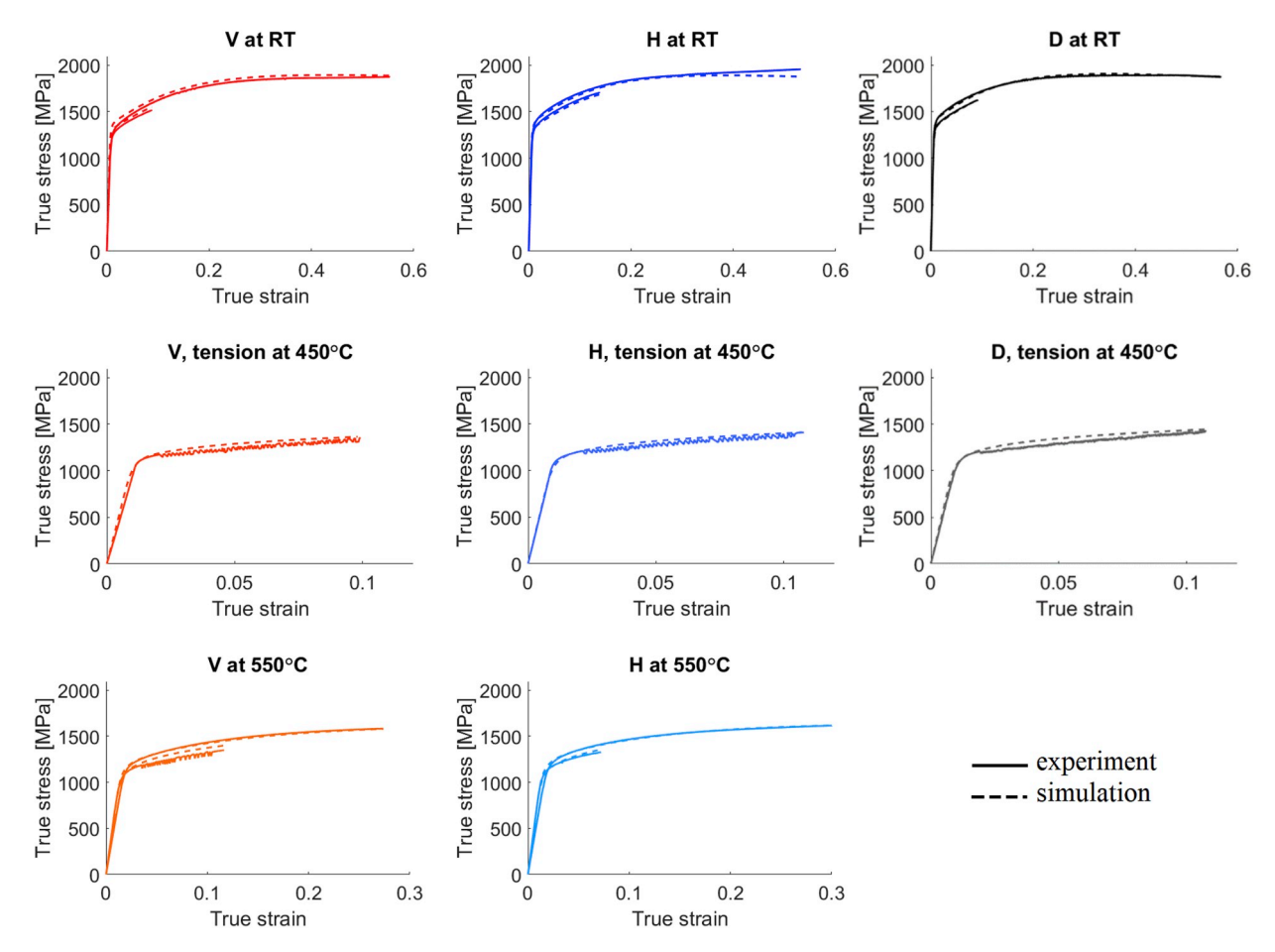


Fig. 5. Comparison of measured and predicted true stress—true strain responses in tension (the shorter curve per plot) and compression (the longer curve per plot) for alloy IN718 as a function of temperature and build direction as indicated in the figure. The measured data is from Fig. 2. Length of the x-axis is different for every row.

where, k_B , $\dot{\varepsilon}_0$, g and D are the Boltzmann constant, a reference strain rate of value $10^7 \, {\rm s}^{-1}$, an effective activation enthalpy and a drag stress, respectively. The drag stress is assumed to be a function of temperature following (Risse et al., 2017). Finally, the increment in debris density $d\rho_{deb}$ depends on the rate of recovery via:

$$d\rho_{deb} = \sum_{s} qb\sqrt{\rho_{deb}}k_2(\dot{\varepsilon}, T)\rho^s_{tot}d\gamma^s$$
 (27)

where q is a coefficient that scales with the fraction of α -type dislocations that are transformed into debris.

4.4. Model setup

Hardening parameters pertaining to the temperature dependent hardening law are identified using part of the mechanical data. These are presented in Table 5. To the authors' knowledge, the high temperature single crystal moduli of this material are not publicly available. The measured single crystal elastic constants for IN718 of $C_{11} = 242.2$ GPa, $C_{12} = 138.9$ GPa, and $C_{44} = 104.2$ GPa (Haldipur, 2006) have been used in the room temperature calculations and softened to match the experimentally measured elastic slope for elevated temperature data. The measured elastic slopes at elevated temperatures are softer than expected for the alloy (Fukuhara and Sanpei, 1993), since the data is presented as measured i.e. without attempting to correct the slopes.

The initial texture used in the simulation is reconstructed from the neutron diffraction pole figure measurements and is represented using 5000 crystal orientations using procedures from (Barrett et al., 2019; Eghtesad et al., 2018; Knezevic and Landry, 2015). Fig. 4 shows pole figures of the initial texture for simulations with respect to the loading direction (LD). The grain shape aspect ratio is set to 5, consistent with the measured grain structure. The simulations are performed in simple compression and tension in three directions relative to the BD: H, V, and D. Consistent with experiments, the imposed strain rate was 10^{-3} s⁻¹.

In this model, we make available only the octahedral $\langle 111 \rangle \langle 1\overline{10} \rangle$ slip mode, since it is the main deformation mode in the service conditions from room temperature to 550 °C. It has been reported experimentally that cubic slip activates at much higher temperatures

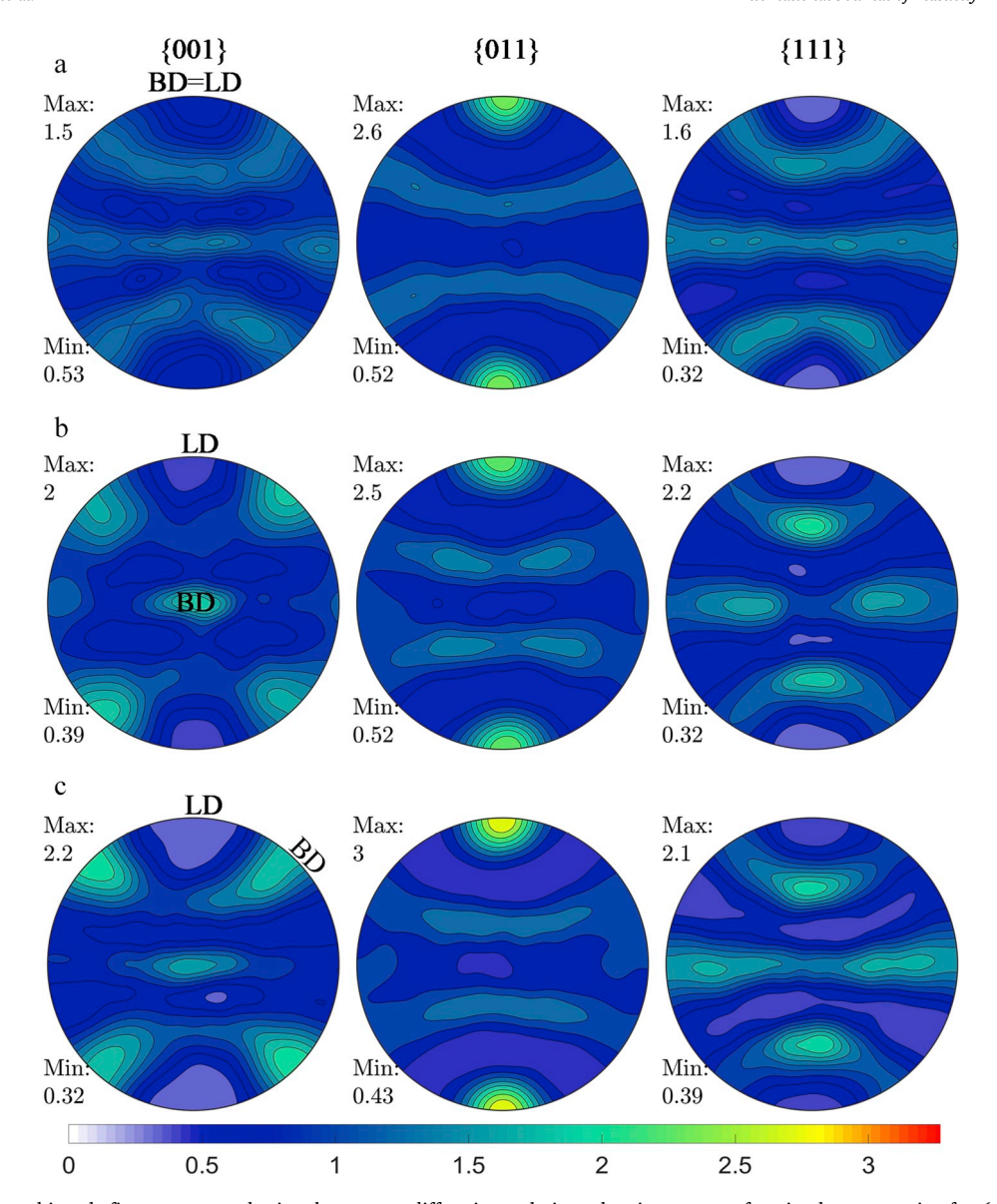


Fig. 6. Stereographic pole figures measured using the neutron diffraction technique showing texture after simple compression for: (a) V, (b) H, and (c) D samples of alloy IN718. The strain values are 0.55, 0.53, and 0.57 respectively. LD is the loading direction, which is vertical. BD is the build direction, which varies.

than considered in this work and therefore, we make available the same octahedral slip systems at all temperatures (Ding et al., 2004; Haddou et al., 2004; Österle et al., 2000; Semiatin et al., 2004).

The final part of developing the model is to characterize the material parameters associated with the hardening model. In earlier work, these parameters were defined for room temperature deformation (Ghorbanpour et al., 2017). Here we identify any temperature dependencies in these parameters by applying the model to a range of temperature, from room to high-temperature deformation of the alloy IN718.

The latent hardening interaction matrix used in Eq. (23) is based on notation in (Franciosi and Zaoui, 1982) with the values from (Devincre et al., 2006; Hoc et al., 2004), which were obtained using dislocation dynamic simulations. The values are $a_0 = 0.068$, $a_1 = 0.068$, $a_2 = 0.0454$, $a_3 = 0.625$, $a_4 = 0.137$, and $a_5 = 0.122$ and correspond to the self-interaction, coplanar interaction, Hirth, collinear, Glissile, and Lomer interaction coefficients, respectively. The matrix is explicitly defined in (Ghorbanpour et al., 2017).

5. Modeling results and discussion

Fig. 5 compares measured and simulated data. As shown, the model achieves agreement in the yield stress, flow stress, and hardening rate for all cases and temperatures. In particular, the calculated response has the same T-C asymmetry, anisotropy, and

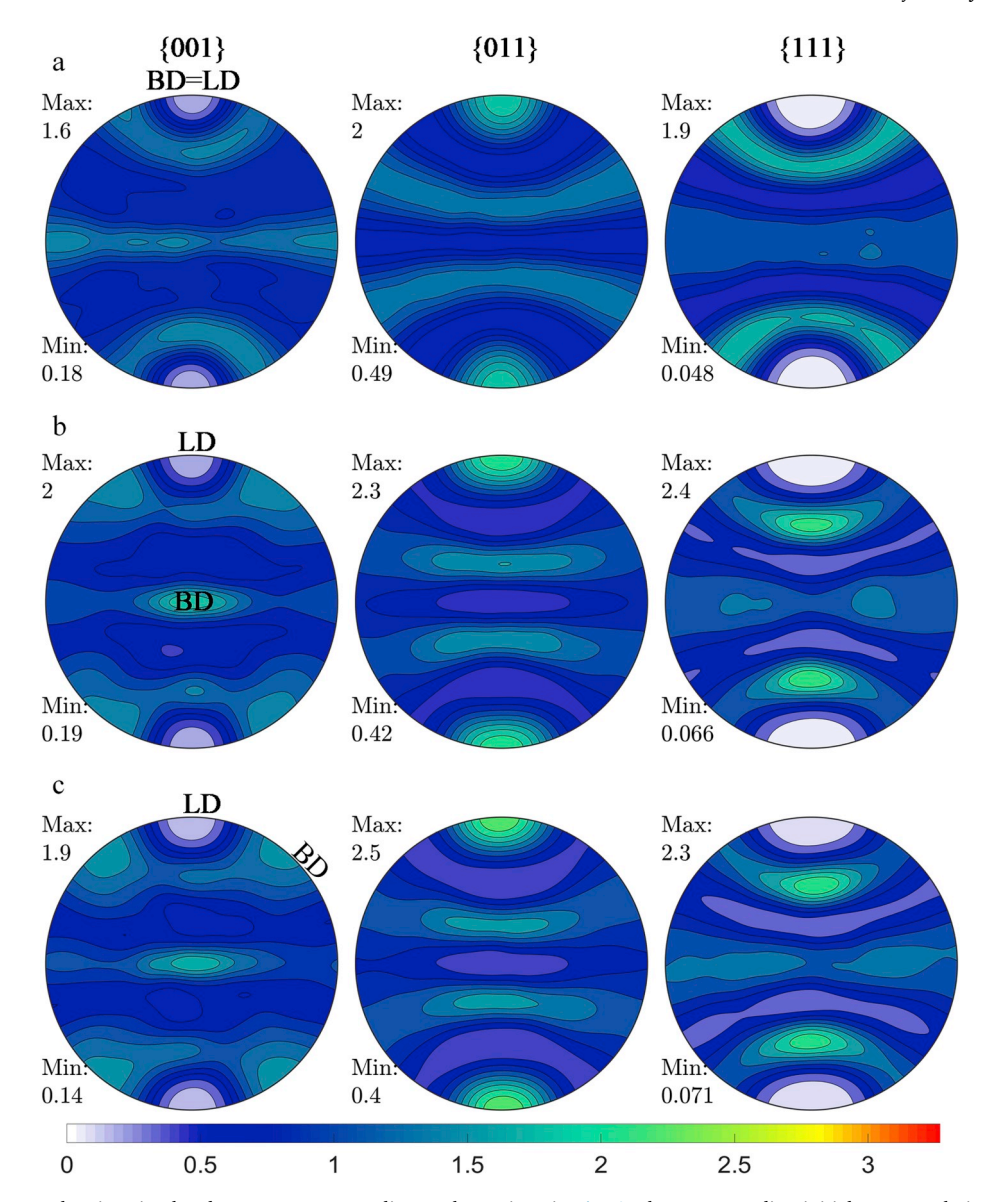


Fig. 7. Pole figures showing simulated textures corresponding to those given in Fig. 6. The corresponding initial texture relative to LD for each simulation case is given in Fig. 4.

hardening rate as the measurement. More importantly, changes in these features with an increase in temperature agree with the measured responses.

Figs. 6 and 7 compare the measured and calculated texture after deformation. Earlier works (Knezevic et al., 2014a, 2014b) have shown no appreciable difference in texture evolution between RT and elevated temperature in materials deforming by the same slip modes at RT and elevated temperatures. Thus, the texture was measured only for the deformed samples experiencing the largest amount of strain to evaluate texture evolution. From the measurements, we observe that for all three samples, H, V, and D, a strong <011> fiber texture formed along the loading direction, which is common for FCC metals. The model achieves an excellent agreement with the measurements.

With a single set of parameters, the model was able to predict the stress-strain response in three build directions, both tension and compression and for three temperatures (for cases when data is available). The analysis finds that not all slip hardening-related parameters are dependent on temperature. It is suggested that the observed decrease in the yield and flow stress with increase in temperature can be understood by a decrease in the initial slip resistance. Table 5 contains the empirical relationships for $\tau_0(T)$ and D(T) used in the calculations shown in Fig. 5. The remaining parameters governing statistical trapping of dislocations, activation enthalpy for recovery processes, and latent hardening parameters could remain temperature independent.

At both RT and 550 C, the alloy exhibits a T-C asymmetry in yield stress, where the yield stress in compression is consistently higher than that in tension. The two components of the model responsible for the T-C asymmetry in the calculated response are the latent

hardening parameters and non-Schmid coefficients with the latter having a dominant effect. Three coefficients, c_2 , c_3 , and c_4 , can lead to a T-C asymmetry (Savage et al., 2017). In this work, we elected to vary only c_1 and c_2 NS coefficients since these coefficients have been associated with separation between the super-partials and Shockley partial separation (Baudouin et al., 2013; Steinmann et al., 1998). Interestingly, the model suggests that $c_1 = 0.045$ is very small in magnitude and insensitive to temperature, whereas the c_2 is much larger in magnitude. Furthermore, c_2 is found to decrease with temperature from 0.97 at RT to 0.75 at 450 °C to 0.3 at 550 °C, indicating that temperature reduces the effect of the $t \otimes n$ non-Schmid resolved shear stress term and hence the evolution of T-C asymmetry. Similar findings have been reported for tantalum in (Zecevic and Knezevic, 2018b).

6. Conclusions

In this work, we studied the mechanical response of alloy IN718 as a function of the initial microstructure created by DMLM, subsequent HIP, and wrought manufacturing. The high temperature stress-strain responses for the alloy in the three DMLM and wrought conditions are provided for the first time. Serrated response is seen for all three DMLM samples tested in tension at 450 °C, and only for DMLM-V sample tested in tension at 550 °C, with variable spacing and stress-amplitude. A critical strain required to initiate the serrated response is ~0.02 at 450 °C, while ~0.035 for DMDL-V at 550 °C. Furthermore, serration is observed for wrought samples tested in compression at 550 °C but interestingly not for the DMLM samples tested at the same temperature in compression. The modeling is carried out only for the DMLM materials in function of the deposition direction and temperature. An elasto-plastic crystal plasticity model is extended to predict the temperature-dependent deformation of DMLM alloy IN718. The model predicts hardening and texture evolution for several test directions across a range of temperatures. The model suggests that anisotropy stems from grain structure, while tension/compression asymmetry predominantly from non-Schmid activation and some from latent hardening.

Acknowledgments

This research was sponsored by the U.S. Army Research Laboratory and was accomplished under Cooperative agreement no. W911NF-15-2-0084. I. J. B and M.E.A. acknowledge financial support from the National Science Foundation (NSF CMMI-1728224). A. K. and I. J. B. acknowledge support from the Center for Scientific Computing from the CNSI, MRL: an NSF MRSEC (DMR-1121053).

Appendix A. Supplementary data

Supplementary data to this article can be found online at https://doi.org/10.1016/j.ijplas.2019.09.002.

References

ASTM E8/E8M-13, 2013. Standard Test Methods for Tension Testing of Metallic Materials. ASTM International, West Conshohocken, PA.

ASTM E9-09, 2018. Standard Test Methods of Compression Testing of Metallic Materials at Room Temperature. ASTM International, West Conshohocken, PA. ASTM E209, 2018. Standard Practice for Compression Tests of Metallic Materials at Elevated Temperatures with Conventional or Rapid Heating Rates and Strain Rates. ASTM International, West Conshohocken, PA.

Amato, K., Gaytan, S., Murr, L., Martinez, E., Shindo, P., Hernandez, J., Collins, S., Medina, F., 2012. Microstructures and mechanical behavior of Inconel 718 fabricated by selective laser melting. Acta Mater. 60, 2229–2239.

Antolovich, S.D., 2015. Microstructural aspects of fatigue in Ni-base superalloys. Phil. Trans. R. Soc. Lond. A: Math. Phys. Eng. Sci. 373, 20140128.

Ardeljan, M., Beyerlein, I.J., Knezevic, M., 2014. A dislocation density based crystal plasticity finite element model: application to a two-phase polycrystalline HCP/BCC composites. J. Mech. Phys. Solids 66, 16–31.

Ardeljan, M., Beyerlein, I.J., Knezevic, M., 2017. Effect of dislocation density-twin interactions on twin growth in AZ31 as revealed by explicit crystal plasticity finite element modeling. Int. J. Plast. 99, 81–101.

Ardeljan, M., Beyerlein, I.J., McWilliams, B.A., Knezevic, M., 2016. Strain rate and temperature sensitive multi-level crystal plasticity model for large plastic deformation behavior: application to AZ31 magnesium alloy. Int. J. Plast. 83, 90–109.

Ardeljan, M., Knezevic, M., 2018. Explicit modeling of double twinning in AZ31 using crystal plasticity finite elements for predicting the mechanical fields for twin variant selection and fracture analyses. Acta Mater. 157, 339–354.

Ardeljan, M., Knezevic, M., Nizolek, T., Beyerlein, I.J., Mara, N.A., Pollock, T.M., 2015. A study of microstructure-driven strain localizations in two-phase polycrystalline HCP/BCC composites using a multi-scale model. Int. J. Plast. 74, 35–57.

Barrett, T.J., Eghtesad, A., McCabe, R.J., Clausen, B., Brown, D.W., Vogel, S.C., Knezevic, M., 2019. A generalized spherical harmonics-based procedure for the interpolation of partial datasets of orientation distributions to enable crystal mechanics-based simulations. Materialia 6, 100328.

Barrett, T.J., Knezevic, M., 2019. Deep drawing simulations using the finite element method embedding a multi-level crystal plasticity constitutive law: experimental verification and sensitivity analysis. Comput. Methods Appl. Mech. Eng. 354, 245–270.

Barrett, T.J., Savage, D.J., Ardeljan, M., Knezevic, M., 2018. An automated procedure for geometry creation and finite element mesh generation: application to explicit grain structure models and machining distortion. Comput. Mater. Sci. 141, 269–281.

Baudouin, J.-B., Monnet, G., Perez, M., Domain, C., Nomoto, A., 2013. Effect of the applied stress and the friction stress on the dislocation dissociation in face centered cubic metals. Mater. Lett. 97, 93–96.

Beese, A.M., Wang, Z., Stoica, A.D., Ma, D., 2018. Absence of dynamic strain aging in an additively manufactured nickel-base superalloy. Nat. Commun. 9, 2083. Bhattacharyya, A., Knezevic, M., Abouaf, M., 2015. Characterization of crystallographic texture and intra-grain morphology in cross-rolled tantalum. Metall. Mater. Trans. A 46, 1085–1096.

Blöchl, P.E., 1994. Projector augmented-wave method. Phys. Rev. B 50, 17953.

Cai, Y., Tian, C., Zhang, G., Han, G., Yang, S., Fu, S., Cui, C., Zhang, Q., 2017. Influence of γ' precipitates on the critical strain and localized deformation of serrated flow in Ni-based superalloys. J. Alloy. Comp. 690, 707–715.

Copley, S., Kear, B., 1967. A dynamic theory of coherent precipitation hardening with application to nickel-base alloys (Coherent precipitation hardening theory treats yielding in nickel base alloy containing coherent stress-free ordered particles as dynamic process). AIME Trans. 239, 984–992.

- Copley, S., Kear, B., 1967. Temperature and orientation dependence of the flow stress in off-stoichiometric Ni sub 3 Al/gamma' phase/(Strength characteristics of single crystals of nickel aluminide/gamma phase/, discussing temperature and orientation dependence of work hardening). AIME Trans. 239, 977–984.
- Courtney, T.H., 1990. Strengthening of Crystalline Materials, Mechanical Behavior of Materials.
- Dao, M., Asaro, R.J., 1993. Non-Schmid effects and localized plastic flow in intermetallic alloys. Mater. Sci. Eng. A 170, 143-160.
- Devincre, B., Kubin, L., Hoc, T., 2006. Physical analyses of crystal plasticity by DD simulations. Scr. Mater. 54, 741-746.
- Ding, Z., Liu, Y., Yin, Z., Yang, Z., Cheng, X., 2004. Study of elastoplastic constitutive model for single crystal nickel-based superalloy. J. Aerosp. Power 19, 755–761.
- Eghtesad, A., Barrett, T.J., Knezevic, M., 2018. Compact reconstruction of orientation distributions using generalized spherical harmonics to advance large-scale crystal plasticity modeling: verification using cubic, hexagonal, and orthorhombic polycrystals. Acta Mater. 155, 418–432.
- Eshelby, J.D., 1957. The determination of the elastic field of an ellipsoidal inclusion, and related problems. Proc. R. Soc. Lond. 241, 376-396.
- Estevez, R., Hoinard, G., Franciosi, P., 1997. Hardening anisotropy of γγ' superalloy single crystals—II. Numberical analysis of heterogeneity effects. Acta Mater. 45, 1567–1584.
- Evans, N., Maziasz, P., Swindeman, R., Smith, G., 2004. Microstructure and phase stability in INCONEL alloy 740 during creep. Scr. Mater. 51, 503–507.
- Ferreri, N.C., Savage, D.J., Vogel, S.C., Knezevic, M., 2019. Unusual phase content in additively manufactured Inconel 718 as revealed by neutron diffraction identification procedures. Acta Mater.
- Franciosi, P., Zaoui, A., 1982. Multislip in f.c.c. crystals a theoretical approach compared with experimental data. Acta Metall. 30, 1627-1637.
- Francis, E.M., Grant, B.M.B., Fonseca, J.Q.d., Phillips, P.J., Mills, M.J., Daymond, M.R., Preuss, M., 2014. High-temperature deformation mechanisms in a polycrystalline nickel-base superalloy studied by neutron diffraction and electron microscopy. Acta Mater. 74, 18–29.
- Fukuhara, M., Sanpei, A., 1993. Elastic moduli and internal frictions of Inconel 718 and Ti-6Al-4V as a function of temperature. J. Mater. Sci. Lett. 12, 1122–1124. Ghorbanpour, S., McWilliams, B.A., Knezevic, M., 2019. Effect of hot working and aging heat treatments on monotonic, cyclic, and fatigue behavior of WE43 magnesium alloy. Mater. Sci. Eng. A 747, 27–41.
- Ghorbanpour, S., McWilliams, B.A., Knezevic, M., 2019. Low-cycle fatigue behavior of rolled WE43-T5 magnesium alloy. Fatigue Fract. Eng. Mater. Struct. 42, 1357–1372.
- Ghorbanpour, S., Zecevic, M., Kumar, A., Jahedi, M., Bicknell, J., Jorgensen, L., Beyerlein, I.J., Knezevic, M., 2017. A crystal plasticity model incorporating the effects of precipitates in superalloys: application to tensile, compressive, and cyclic deformation of Inconel 718. Int. J. Plast. 99, 162–185.
- Gleiter, H., Hornbogen, E., 1968. Precipitation hardening by coherent particles. Mater. Sci. Eng. 2, 285-302.
- Gribbin, S., Bicknell, J., Jorgensen, L., Tsukrov, I., Knezevic, M., 2016. Low cycle fatigue behavior of direct metal laser sintered Inconel alloy 718. Int. J. Fatigue 93 (1), 156–167.
- Gribbin, S., Ghorbanpour, S., Ferreri, N.C., Bicknell, J., Tsukrov, I., Knezevic, M., 2019. Role of grain structure, grain boundaries, crystallographic texture, precipitates, and porosity on fatigue behavior of Inconel 718 at room and elevated temperatures. Mater. Char. 149, 184–197.
- Haddou, H., Risbet, M., Marichal, G., Feaugas, X., 2004. The effects of grain size on the cyclic deformation behaviour of polycrystalline nickel. Mater. Sci. Eng. A 379, 102–111.
- Haldipur, P., 2006. Material Characterization of Nickel-Based Super Alloys through Ultrasonic Inspection. Materials Science and Engineering Iowa State University, Ames, Iowa.
- Hayes, R., Hayes, W., 1984. A proposed model for the disappearance of serrated flow in two Fe alloys. Acta Metall. 32, 259-267.
- Hayes, R.W., Hayes, W.C., 1982. On the mechanism of delayed discontinuous plastic flow in an age-hardened nickel alloy. Acta Metall. 30, 1295-1301.
- Hoc, T., Devincre, B., Kubin, L.P., 2004. Deformation stage I of FCC crystals: constitutive modelling. In: Gundlach, C., Haldrup, K., Hansen, N., Huang, X., Jensen, D.J., Leffers, T., Li, Z.J., Nielsen, S.F., Pantleon, W., Wert, J.A., Winther, G. (Eds.), Proceedings of the 25th Riso International Symposium on Materials Science: Evolution of Deformation Microstructures in 3D. Riso National Laboratory, Roskilde, Denmark.
- Hoinard, G., Estevez, R., Franciosi, P., 1995. Hardening anisotropy of γ/γ' superalloy single crystals—I. Experimental estimates at 650°C from a homogeneous analysis. Acta Metall. Mater. 43, 1593–1607.
- Huther, W., Reppich, B., 1978. Interaction of dislocations with coherent, stree-free ordered particles. Zeitschrift Fur Metallkunde 69, 628-634.
- Iwakuma, T., Nemat-Nasser, S., Hill, R., 1984. Finite elastic-plastic deformation of polycrystalline metals. Proc. R. Soc. Lond. Ser A Math. Phys. Sci. 394, 87–119.
 Jahedi, M., Ardeljan, M., Beyerlein, I.J., Paydar, M.H., Knezevic, M., 2015. Enhancement of orientation gradients during simple shear deformation by application of simple compression. J. Appl. Phys. 117, 214309.
- Jahedi, M., McWilliams, B.A., Moy, P., Knezevic, M., 2017. Deformation twinning in rolled WE43-T5 rare earth magnesium alloy: influence on strain hardening and texture evolution. Acta Mater. 131, 221–232.
- Keshavarz, S., Ghosh, S., 2015. A crystal plasticity finite element model for flow stress anomalies in Ni3Al single crystals. Philos. Mag. 95, 2639-2660.
- Kitayama, K., Tomé, C.N., Rauch, E.F., Gracio, J.J., Barlat, F., 2013. A Crystallographic Dislocation Model for Describing Hardening of Polycrystals during Strain Path Changes. Application to Low Carbon Steels. International Journal of Plasticity in press.
- Knezevic, M., Beyerlein, I.J., Lovato, M.L., Tomé, C.N., Richards, A.W., McCabe, R.J., 2014. A strain-rate and temperature dependent constitutive model for BCC metals incorporating non-Schmid effects: application to tantalum-tungsten alloys. Int. J. Plast. 62, 93–104.
- Knezevic, M., Bhattacharyya, A., 2017. Characterization of microstructure in Nb rods processed by rolling: effect of grooved rolling die geometry on texture uniformity. Int. J. Refract. Metals Hard Mater. 66, 44–51.
- Knezevic, M., Capolungo, L., Tomé, C.N., Lebensohn, R.A., Alexander, D.J., Mihaila, B., McCabe, R.J., 2012. Anisotropic stress-strain response and microstructure evolution of textured α-uranium. Acta Mater. 60, 702–715.
- Knezevic, M., Carpenter, J.S., Lovato, M.L., McCabe, R.J., 2014. Deformation behavior of the cobalt-based superalloy Haynes 25: experimental characterization and crystal plasticity modeling. Acta Mater. 63, 162–168.
- Knezevic, M., Chun, B.K., Oh, J.Y., Wu, W.T., Ress Iii, R.A., Glavicic, M.G., Srivatsa, S., 2012. Modeling Machining Distortion Using the Finite Element Method: Application to Engine Disk, pp. 40–46.
- Knezevic, M., Ghorbanpour, S., 2018. Modeling tensile, compressive, and cyclic response of inconel 718 using a crystal plasticity model incorporating the effects of precipitates. In: Proceedings of the 9th International Symposium on Superalloy 718 & Derivatives: Energy, Aerospace, and Industrial Applications. Springer, pp. 655–668.
- Knezevic, M., Landry, N.W., 2015. Procedures for reducing large datasets of crystal orientations using generalized spherical harmonics. Mech. Mater. 88, 73–86. Knezevic, M., Levinson, A., Harris, R., Mishra, R.K., Doherty, R.D., Kalidindi, S.R., 2010. Deformation twinning in AZ31: influence on strain hardening and texture evolution. Acta Mater. 58, 6230–6242.
- Knezevic, M., McCabe, R.J., Tomé, C.N., Lebensohn, R.A., Chen, S.R., Cady, C.M., Gray Iii, G.T., Mihaila, B., 2013. Modeling mechanical response and texture evolution of α-uranium as a function of strain rate and temperature using polycrystal plasticity. Int. J. Plast. 43, 70–84.
- Knezevic, M., Zecevic, M., Beyerlein, I.J., Bhattacharyya, A., McCabe, R.J., 2015. Predicting texture evolution in Ta and Ta-10W alloys using polycrystal plasticity. J. Occup. Med. 67, 2670–2674.
- Knezevic, M., Zecevic, M., Beyerlein, I.J., Bingert, J.F., McCabe, R.J., 2015. Strain rate and temperature effects on the selection of primary and secondary slip and twinning systems in HCP Zr. Acta Mater. 88, 55–73.
- Knezevic, M., Zecevic, M., Beyerlein, I.J., Lebensohn, R.A., 2016. A numerical procedure enabling accurate descriptions of strain rate-sensitive flow of polycrystals within crystal visco-plasticity theory. Comput. Methods Appl. Mech. Eng. 308, 468–482.
- Kresse, G., Furthmüller, J., 1996. Efficient iterative schemes for ab initio total-energy calculations using a plane-wave basis set. Phys. Rev. B 54, 11169.
- Kresse, G., Hafner, J., 1994. Ab initio molecular-dynamics simulation of the liquid-metal-amorphous-semiconductor transition in germanium. Phys. Rev. B 49, 14251. Kresse, G., Joubert, D., 1999. From ultrasoft pseudopotentials to the projector augmented-wave method. Phys. Rev. B 59, 1758.
- Kuo, C.M., Yang, Y.T., Bor, H.Y., Wei, C.N., Tai, C.C., 2009. Aging effects on the microstructure and creep behavior of Inconel 718 superalloy. Mater. Sci. Eng. A 510–511, 289–294.

Lass, E.A., Stoudt, M.R., Williams, M.E., Katz, M.B., Levine, L.E., Phan, T.Q., Gnaeupel-Herold, T.H., Ng, D.S., 2017. formation of the Ni3Nb δ-phase in stress-relieved inconel 625 produced via laser powder-bed fusion additive manufacturing. Metall. Mater. Trans. A 48, 5547–5558.

Lebensohn, R.A., Tomé, C.N., 1993. A self-consistent anisotropic approach for the simulation of plastic deformation and texture development of polycrystals: application to zirconium alloys. Acta Metall. Mater. 41, 2611–2624.

Li, W., Ma, J., Kou, H., Shao, J., Zhang, X., Deng, Y., Tao, Y., Fang, D., 2019. Modeling the effect of temperature on the yield strength of precipitation strengthening Nibase superalloys. Int. J. Plast. 116, 143–158.

Lim, H., Weinberger, C.R., Battaile, C.C., Buchheit, T.E., 2013. Application of generalized non-Schmid yield law to low-temperature plasticity in bcc transition metals. Model. Simul. Mater. Sci. Eng. 21, 045015.

Lipinski, P., Berveiller, M., 1989. Elastoplasticity of micro-inhomogeneous metals at large strains. Int. J. Plast. 5, 149-172.

Maciejewski, K., Jouiad, M., Ghonem, H., 2013. Dislocation/precipitate interactions in IN100 at 650 °C. Mater. Sci. Eng. A 582, 47-54.

Madec, R., Devincre, B., Kubin, L., Hoc, T., Rodney, D., 2003. The role of collinear interaction in dislocation-induced hardening. Science 301, 1879-1882.

Maj, P., Zdunek, J., Gizynski, M., Mizera, J., Kurzydlowski, K.J., 2014. Statistical analysis of the portevin–le chatelier effect in inconel 718 at high temperature. Mater. Sci. Eng. A 619, 158–164.

Manikandan, S., Sivakumar, D., Rao, K.P., Kamaraj, M., 2015. Laves phase in alloy 718 fusion zone—microscopic and calorimetric studies. Mater. Char. 100, 192–206. Mannan, S., 1993. Role of dynamic strain ageing in low cycle fatigue. Bull. Mater. Sci. 16, 561–582.

Mei, Y., Liu, Y., Liu, C., Li, C., Yu, L., Guo, Q., Li, H., 2015. Effects of cold rolling on the precipitation kinetics and the morphology evolution of intermediate phases in Inconel 718 alloy. J. Alloy. Comp. 649, 949–960.

Mostafa, A., Picazo Rubio, I., Brailovski, V., Jahazi, M., Medraj, M., 2017. Structure, texture and phases in 3D printed IN718 alloy subjected to homogenization and HIP treatments. Metals 7, 196.

Mukherji, D., Gilles, R., Barbier, B., Del Genovese, D., Hasse, B., Strunz, P., Wroblewski, T., Fuess, H., Rösler, J., 2003. Lattice misfit measurement in Inconel 706 containing coherent γ' and γ "precipitates. Scr. Mater. 48, 333–339.

Murr, L.E., Martinez, E., Amato, K.N., Gaytan, S.M., Hernandez, J., Ramirez, D.A., Shindo, P.W., Medina, F., Wicker, R.B., 2012. Fabrication of metal and alloy components by additive manufacturing: examples of 3D materials science. J. Mater. Res. Technol. 1, 42–54.

Murr, L.E., Martinez, E., Gaytan, S., Ramirez, D., Machado, B., Shindo, P., Martinez, J., Medina, F., Wooten, J., Ciscel, D., 2011. Microstructural architecture, microstructures, and mechanical properties for a nickel-base superalloy fabricated by electron beam melting. Metall. Mater. Trans. A 42, 3491–3508.

Neil, C.J., Wollmershauser, J.A., Clausen, B., Tomé, C.N., Agnew, S.R., 2010. Modeling lattice strain evolution at finite strains and experimental verification for copper and stainless steel using in situ neutron diffraction. Int. J. Plast. 26, 1772–1791.

Österle, W., Bettge, D., Fedelich, B., Klingelhöffer, H., 2000. Modelling the orientation and direction dependence of the critical resolved shear stress of nickel-base superalloy single crystals. Acta Mater. 48, 689–700.

Perdew, J.P., Burke, K., Ernzerhof, M., 1996. Generalized gradient approximation made simple. Phys. Rev. Lett. 77, 3865.

Rao, G.A., Kumar, M., Srinivas, M., Sarma, D., 2003. Effect of standard heat treatment on the microstructure and mechanical properties of hot isostatically pressed superalloy inconel 718. Mater. Sci. Eng. A 355, 114–125.

Risse, M., Lentz, M., Fahrenson, C., Reimers, W., Knezevic, M., Beyerlein, I.J., 2017. Elevated temperature effects on the plastic anisotropy of an extruded Mg-4 Wt pct Li alloy: experiments and polycrystal modeling. Metall. Mater. Trans. A 48, 446–458.

Roth, H.A., Davis, C.L., Thomson, R.C., 1997. Modeling solid solution strengthening in nickel alloys. Metall. Mater. Trans. A 28, 1329–1335.

Savage, D.J., Beyerlein, I.J., Knezevic, M., 2017. Coupled texture and non-Schmid effects on yield surfaces of body-centered cubic polycrystals predicted by a crystal plasticity finite element approach. Int. J. Solids Struct. 109, 22–32.

Savage, D.J., Chandola, N., Cazacu, O., McWilliams, B.A., Knezevic, M., 2018. Validation of recent analytical dilatational models for porous polycrystals using crystal plasticity finite element models with Schmid and non-Schmid activation laws. Mech. Mater. 126, 148–162.

Schmid, E., Boas, W., 1950. Plasticity of Crystals with Special Reference to Metals. English translation F.A. Hughes, London.

Semiatin, S., Fagin, P., Glavicic, M., Raabe, D., 2004. Deformation behavior of Waspaloy at hot-working temperatures. Scr. Mater. 50, 625-629.

Shenoy, M., Tjiptowidjojo, Y., McDowell, D., 2008. Microstructure-sensitive modeling of polycrystalline IN 100. Int. J. Plast. 24, 1694–1730.

Slama, C., Abdellaoui, M., 2000. Structural characterization of the aged Inconel 718. J. Alloy. Comp. 306, 277–284.

Sleeswyk, A., 1958. Slow strain-hardening of ingot iron. Acta Metall. 6, 598-603.

Smith, D.H., Bicknell, J., Jorgensen, L., Patterson, B.M., Cordes, N.L., Tsukrov, I., Knezevic, M., 2016. Microstructure and mechanical behavior of direct metal laser sintered Inconel alloy 718. Mater. Char. 113, 1–9.

Steinmann, P., Kuhl, E., Stein, E., 1998. Aspects of non-associated single crystal plasticity: influence of non-Schmid effects and localization analysis. Int. J. Solids Struct. 35, 4437–4456.

Turner, P.A., Tomé, C.N., 1994. A study of residual stresses in Zircaloy-2 with rod texture. Acta Metall. Mater. 42, 4143-4153.

Umakoshi, Y., Pope, D.P., Vitek, V., 1984. The asymmetry of the flow stress in Ni3(Al,Ta) single crystals. Acta Metall. 32, 449-456.

Weaver, M., Hale, C., 2001. Effects of precipitation on serrated yielding in Inconel 718. Superalloys 718, 625-706.

Xiao, L., Chen, D.L., Chaturvedi, M.C., 2005. Shearing of γ" precipitates and formation of planar slip bands in Inconel 718 during cyclic deformation. Scr. Mater. 52, 603–607.

Zecevic, M., Beyerlein, I.J., Knezevic, M., 2017. Coupling elasto-plastic self-consistent crystal plasticity and implicit finite elements: applications to compression, cyclic tension-compression, and bending to large strains. Int. J. Plast. 93, 187–211.

Zecevic, M., Knezevic, M., 2015. A dislocation density based elasto-plastic self-consistent model for the prediction of cyclic deformation: application to Al6022-T4. Int. J. Plast. 72, 200–217.

Zecevic, M., Knezevic, M., 2017. Modeling of sheet metal forming based on implicit embedding of the elasto-plastic self-consistent formulation in shell elements: application to cup drawing of AA6022-T4. J. Occup. Med. 69, 922–929.

Zecevic, M., Knezevic, M., 2018. Latent hardening within the elasto-plastic self-consistent polycrystal homogenization to enable the prediction of anisotropy of AA6022-T4 sheets. Int. J. Plast. 105, 141–163.

Zecevic, M., Knezevic, M., 2018. A new visco-plastic self-consistent formulation implicit in dislocation-based hardening within implicit finite elements: application to high strain rate and impact deformation of tantalum. Comput. Methods Appl. Mech. Eng. 341, 888–916.

Zecevic, M., Knezevic, M., 2019. An implicit formulation of the elasto-plastic self-consistent polycrystal plasticity model and its implementation in implicit finite elements. Mech. Mater. 136, 103065.

Zecevic, M., Upadhyay, M.V., Polatidis, E., Panzner, T., Van Swygenhoven, H., Knezevic, M., 2019. A crystallographic extension to the Olson-Cohen model for predicting strain path dependence of martensitic transformation. Acta Mater. 166, 386–401.